Research Article | Vol. 25, No. 26 | 25 Dec 2017 | OPTICS EXPRESS 33559
Optics EXPRESS

Centroid error compensation method for a star tracker under complex dynamic conditions

WENFENG TAN,[1,2] SHIQIAO QIN,[1,3] R. M. MYERS,[2] T. J. MORRIS,[2] GUANGWEN JIANG,[1] YINGWEI ZHAO,[1] XINGSHU WANG,[1] LIHENG MA,[1] AND DONGKAI DAI[1,*]

[1] *College of Opto-Electronic Science and Engineering, National University of Defense Technology, Changsha 410073, China*
[2] *Centre for Advanced Instrumentation, Durham Univ., South Road, Durham, DH1 3LE, UK*
[3] *sqqin8@nudt.edu.cn*
[*] *daidongkai@nudt.edu.cn*

Abstract: The traditional approach of a star tracker for reducing the dynamic error concentrates on a single frame of star images. Through correlating adjacent star images together with their angular relations sensed by a gyroscope unit (GU), the attitude-correlated frames (ACF) approach expands the view from one single frame to frame sequences. However, the star centroid is shifted from the star true position at the center time of the exposure period under complex dynamic conditions, which is called the complex motion induced error (CMIE) in this paper. The CMIE has a large effect on the performance of the ACF approach. This paper presents a method to compensate the CMIE through reconstructing the star trajectory with the angular velocity of the star tracker sensed by a GU, which achieves effective compensation of the CMIE crossing the boresight direction. Since the observation sensitivity to the CMIE along the boresight direction is low, the attitudes from two different fields of view (FOVs) are combined to improve its compensation accuracy. Then the ACF approach is applied to the obtained results where the CMIE has already been compensated completely. Simulations under shipboard dynamic conditions and experiments under oscillating conditions indicate that the proposed method is effective in improving the performance of the ACF approach and reducing the dynamic error of a star tracker under complex dynamic conditions.

OCIS codes: (120.4640) Optical instruments; (100.4145) Motion, hyperspectral image processing;(120.6085) Space instrumentation; (280.4788) Optical sensing and sensors.

References and links

1. C. Liu, G. Liu, X. Wang and A. Li, *Principles and Systematic Applications of Missile-Borne Star Sensor* (National Defense Industry, 2010).
2. J. L. Jorgensen, T. Denver, M. Betto, and P. V. d. Braembussche, "The PROBA satellite star tracker performance," Acta Astronautica **56**, 153–159 (2005).
3. R. W. H. v. Bezooijen, "SIRTF autonomous star tracker," in *Astronomical Telescopes and Instrumentation* (SPIE, 2003), 14.
4. W. Zhang, W. Quan, and L. Guo, "Blurred Star Image Processing for Star Sensors under Dynamic Conditions," Sensors **12**, 6712 (2012).
5. K. Wang, C. Zhang, Y. Li, and X. Kan, "A New Restoration Algorithm for the Smeared Image of a SINS-aided Star Sensor," Journal of Navigation **67**, 881–898 (2014).
6. W. Quan, and W. Zhang, "Restoration of Motion-blurred Star Image Based on Wiener Filter," in *2011 International Conference on Intelligent Computation Technology and Automation* (IEEE, 2011), pp. 691–694.
7. T. Sun, F. Xing, Z. You, X. Wang, and B. Li, "Smearing model and restoration of star image under conditions of variable angular velocity and long exposure time," Opt. Express **22**, 6009–6024 (2014).
8. F. Xing, N. Chen, Z. You, and T. Sun, "A Novel Approach Based on MEMS-Gyro's Data Deep Coupling for Determining the Centroid of Star Spot," Math. Probl. Eng. **2012**, 403584(2012).
9. S. Qin, D. Zhan, J. Zheng, W. Wu, H. Jia, S. Fu and L. Ma, "Dynamic attitude measurement method of star sensor based on gyro's precise angular correlation," U.S. Patent 9,316,716 (2016).

#312733 https://doi.org/10.1364/OE.25.033559
Journal © 2017 Received 8 Nov 2017; revised 19 Dec 2017; accepted 19 Dec 2017; published 22 Dec 2017

Optics EXPRESS

10. L. Ma, D. Zhan, G. Jiang, S. Fu, H. Jia, X. Wang, Z. Huang, J. Zheng, F. Hu, W. Wu, and S. Qin, "Attitude-correlated frames approach for a star sensor to improve attitude accuracy under highly dynamic conditions," Appl. Opt. **54**, 7559–7566 (2015).
11. J. Jiang, J. Huang, and G. Zhang, "An Accelerated Motion Blurred Star Restoration Based on Single Image," IEEE Sensors Journal **17**, 1306–1315 (2017).
12. R. A. Fowell, S. I. Saeed, R. Li and Y.-W. A. Wu, "Mitigation of angular acceleration effects on optical sensor data," U.S. Patent 6, 863, 244 (2005).
13. R. A. Fowell, R. Li and Y.-W. A. Wu, "Method for compensating star motion induced error in a stellar inertial attitude determination system," U.S. Patent 7, 487, 016 (2009).
14. T. Sun, F. Xing, X. Wang, Z. You, and D. Chu, "An accuracy measurement method for star trackers based on direct astronomic observation," Sci. Rep. **6**, 22593 (2016).
15. G. Wahba, "A Least Squares Estimate of Satellite Attitude," SIAM Rev. **7**, 409 (1965).
16. C. C. Liebe, "Accuracy performance of star trackers - a tutorial," IEEE Trans. Aerosp. Electron. Syst. **38**(2), 587–599 (2002).
17. D. Titterton, and J. L. Weston, *Strapdown inertial navigation technology* (IET, 2004).
18. L. Ma, F. Bernelli-Zazzera, S. Qin and X. Wang, "Performance analysis of the attitude-correlated frames approach for star sensors," in *2016 IEEE Metrology for Aerospace (MetroAeroSpace)* (IEEE, 2016), pp. 81–86.
19. L. Ma, C. Hu, X. Wang, and D. Dai, "Advances and accuracy performance of the star trackers," in *ISPDI 2013 - Fifth International Symposium on Photoelectronic Detection and Imaging* (SPIE, 2013), 9.
20. J. Hua, T. Zhang, and H. Zhu, "Star image fusion and star recognition of multi-FOV star sensor," in *Proceedings of 2014 IEEE Chinese Guidance, Navigation and Control Conference* (IEEE, 2014), pp. 2111–2125.
21. J. Yan, J. Jiang, and G. Zhang, "Dynamic imaging model and parameter optimization for a star tracker," Opt. Express **24**, 5961–5983 (2016).

1. Introduction

As an absolute attitude determination device, a star tracker can provide highly accurate attitude information for vehicles e.g. satellites, ballistic missiles and ships etc. It can be integrated with other navigation devices e.g. an inertial navigation system (INS) to improve the performance of integrated navigation systems. It is widely used in the fields of attitude determination, guidance and navigation [1, 2]. However, the attitude measurement accuracy of a star tracker declines under dynamic conditions such as the satellite attitude maneuvering or the ship motion. In such a dynamic condition, stellar images will become motion-blurred. The star centroid accuracy will also decrease, leading to the rapid degradation of the attitude measurement accuracy [3]. Therefore, current researches mainly focus on improving the star tracker attitude measurement accuracy under dynamic conditions.

To improve the attitude accuracy of a star tracker under dynamic conditions, star restoration algorithms [4–7] and centroid compensation algorithms [8–10] are widely researched. Zhang et al. [4], Wang et al. [5] and Quan et al. [6] applied Wiener filtering to restore the motion-blurred star image, which was always accompanied by serious ringing effect. Sun et al. [7] employed the Lucy-Richardson (LR) reconstruction that effectively restrained the ringing phenomenon [11]. Using this method, the star centroid accuracy can be maintained in the range of 0.62 pixels (3σ) under dynamic conditions of $4.989^\circ/s$. Jiang et al. proposed an accelerated LR restoration algorithm, offering speedup of 20 times over the original LR and 5 times over the existing acceleration algorithms [11]. Different from the star restoration method, centroid compensation algorithms can be applied to compensate the error of the star centroid obtained through direct extraction. Xing et al. [8] adopted the Extended Kalman filter (EKF) for the star centroid determination. The centroid error was about 1 pixel with an angular velocity of $8^\circ/s$ for a star with a magnitude of 5 in the simulation. The attitude-correlated frames (ACF) approach was proposed by Qin et al. [9], which expanded the view from one single frame to frame sequences. With the angular relations sensed by a gyroscope unit (GU), which consists of three orthogonally assembled gyroscopes, the adjacent frames were correlated together to restrain the random error of the star tracker. With ACF approach, the star tracker accuracy can be improved by a factor of $\sqrt{N}$ where N refers to the number of correlated frames as introduced in [9, 10].

The centroid error requires a Gaussian distribution for the application of the ACF approach.

Optics EXPRESS

The effectiveness of the ACF approach has been verified under conditions when angular velocity is quasi-static during the exposure period [10]. However, under complex dynamic conditions when the angular velocity of a vehicle continuously varies during the exposure period, the measured centroid will be shifted from the star true position in the center of the exposure period [12, 13]. Accordingly, the centroid error no longer follows a Gaussian distribution, but a distribution related to the motion characteristics of the star tracker. In other words, the correlation matrices between adjacent frames cannot be calculated accurately due to the uncertainty on the time tags of these frames caused by complex motion. Taking a shipborne star tracker for an example, its angular velocity changes quickly during an exposure period due to the wind wave and ocean swell, which causes the complex motion induced error (CMIE) in centroid determination. In such a condition, the performance of the ACF approach is limited because of complex motion. In this paper, a method of compensating the CMIE of a star tracker under complex dynamic conditions is proposed. The ACF approach is then applied to improve the attitude accuracy further. Both simulation of shipboard dynamic conditions and night-sky experiment validate this method. The simulation and experimental results demonstrate that the proposed method can improve the dynamic accuracy of a star tracker in complex dynamic conditions.

This paper is organized as follows. In Section 2, the ACF approach is reintroduced briefly, and the limitations of the ACF approach under complex dynamic conditions are analyzed. In Section 3, the centroid error compensation method under complex dynamic conditions is explained. Simulation and experimental results are presented in Section 4 and Section 5 respectively. Finally, conclusions are presented in Section 6.

2. ACF approach under complex dynamic conditions

2.1. Reference coordinate system definition

The coordinate systems used in this paper are defined as follows:

The Earth-centered inertial coordinate system (represented by i) is fixed in inertial space and centered on the Earth. Its X_i axis is in the equatorial plane and points to the vernal equinox. The Z_i axis is aligned with the Earth's rotation axis and vertical to the equatorial plane. The Y_i axis completes a right-handed frame as shown in Fig. 1.

The image plane coordinate system (represented by p) is a two-dimensional rectangular plane coordinate system with its origin at the detector center, and its X_p and Y_p axes are parallel to a row and a column of the detector respectively.

The star tracker coordinate system (represented by s) has its origin at the detector center. The X_s and Y_s axes are parallel to a row and a column of the detector, respectively. The Z_s, X_s and Y_s axes satisfy the right-hand rule [14] as shown in Fig. 1.

The computed star tracker coordinate system (represented by s') deviates from the true star tracker coordinate system due to attitude measurement error. It can be obtained by rotating a certain Euler angle of the s frame.

The gyroscope unit coordinate system (represented by g) has its X_g, Y_g and Z_g axes consistent with the three mutually orthogonal sensitive axes of the gyroscope unit as shown in Fig. 1.

2.2. Principles of ACF approach

Star images recorded at different time epochs and in different angular positions can be correlated through attitude transformations, calculated by GU outputs [10]. The principle of ACF approach is depicted in detail in [9, 10]. The main formulas of ACF approach are re-presented in this paper briefly.

In each star image, the observed vectors in the s frame, $\mathbf{S}^j = \left[\mathbf{s}_1^j, \mathbf{s}_2^j, \cdots, \mathbf{s}_{n_{star}}^j\right]$, and the reference vectors in the i frame, $\mathbf{P}^j = \left[\mathbf{p}_1^j, \mathbf{p}_2^j, \cdots, \mathbf{p}_{n_{star}}^j\right]$ can be obtained through star centroid

Optics EXPRESS

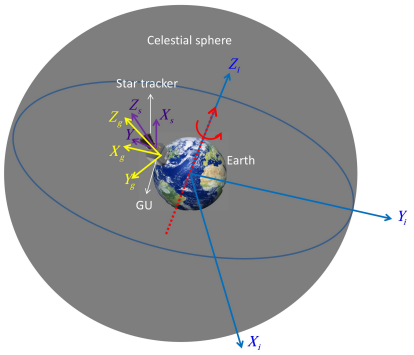

Fig. 1. Definition of coordinate systems.

extraction and star identification [10] (j is the star image index number satisfying $j = 1, 2, \cdots, N$, and n_{star} is the number of stars in the j-th star image). Here, $\mathbf{S}^j$ and $\mathbf{P}^j$ satisfy the Wahba equation [15]:

$$\begin{cases} \mathbf{P}^1 = \mathbf{C}_1^i \mathbf{S}^1 + \mathbf{E}^1 \\ \mathbf{P}^2 = \mathbf{C}_2^i \mathbf{S}^2 + \mathbf{E}^2 \\ \quad\quad \vdots \\ \mathbf{P}^N = \mathbf{C}_N^i \mathbf{S}^N + \mathbf{E}^N \end{cases}, \tag{1}$$

where $\mathbf{C}_1^i$, $\mathbf{C}_2^i$ and $\mathbf{C}_N^i$ are the attitude matrices from s frame to i frame at time epochs t_1, t_2 and t_N respectively, and t_j is the center of the exposure period in the j-th frame. $\mathbf{E}^1$, $\mathbf{E}^2$ and $\mathbf{E}^N$ are the measurement errors of the star tracker caused by the detector noise. Generally, attitude matrices can be optimally estimated through subformulas in Eq. (1) independently. The cross boresight noise equivalent angle (NEA) error E_{ss} can be calculated by [16]:

$$E_{ss} = \frac{FOV}{n_{pixel}} \cdot \frac{E_{centroid}}{\sqrt{\overline{n}_{star}}}, \tag{2}$$

where FOV is field of view of the star tracker in degrees, n_{pixel} is the number of pixels across the focus plane, $E_{centroid}$ is the average centroiding accuracy, and $\overline{n}_{star}$ is the average number of detected stars in the camera image [16]. According to Eq. (2), the NEA error is inversely proportional to $\sqrt{\overline{n}_{star}}$.

The angular variation of adjacent frames are measured by a GU. The attitude transformations from j-th frame to N-th frame, $\mathbf{G}_j^N$ can be calculated through an attitude updating algorithm [17] with angular increments sensed by the GU. Accordingly, subformulas in Eq. (1) can be correlated into a single one [18]:

$$\begin{cases} \left[\mathbf{P}^1, \mathbf{P}^2, \cdots, \mathbf{P}^N\right] = \mathbf{C}_N^i \left[\mathbf{G}_1^N \mathbf{S}^1, \mathbf{G}_2^N \mathbf{S}^2, \cdots, \mathbf{S}^N\right] + \left[\mathbf{E}^1, \mathbf{E}^2, \cdots, \mathbf{E}^N\right] \\ \mathbf{G}_j^N = \prod_{l=j}^{l=N-1} \mathbf{G}_l^{l+1}, j = 1, 2, \cdots, N-1 \end{cases}. \tag{3}$$

According to Eq. (3), the number of stars for the attitude matrix estimation are multiplied by N. So the NEA error will be reduced by a factor of $1/\sqrt{N}$ [18].

A simplified solution algorithm named as the average optimal solution can be used to reduce the computation load [9]. The average optimal solution $\bar{\hat{\mathbf{C}}}_N^i$ of the N-th frame can be calculated as follows [9]:

$$\bar{\hat{\mathbf{C}}}_N^i = \frac{1}{N}\left[\hat{\mathbf{C}}_N^i + \hat{\mathbf{C}}_{N-1}^i \mathbf{G}_N^{N-1} + \cdots + \left(\hat{\mathbf{C}}_1^i \mathbf{G}_2^1 \mathbf{G}_3^2 \cdots \mathbf{G}_N^{N-1}\right)\right], \tag{4}$$

where $\hat{\mathbf{C}}_N^i, \hat{\mathbf{C}}_{N-1}^i, \cdots, \hat{\mathbf{C}}_1^i$ are the single-frame optimal attitude matrices calculated by subformulas in Eq. (1).

2.3. Effect of CMIE on ACF approach

When applying the ACF algorithm, the observed vectors in the s frame at time epoch t_j, $\mathbf{S}^j$, will be transformed to new vectors at time epoch t_N through the attitude transformation $\mathbf{G}_j^N$. The correlation equation is as follows:

$$\hat{\mathbf{S}}_j^N = \mathbf{G}_j^N \mathbf{S}^j + \mathbf{E}^j. \tag{5}$$

Here, $\hat{\mathbf{S}}_j^N$ represents the results after correlating the observed vectors from t_j to t_N. However, the observed vectors will be shifted from the star true position at the center time of the exposure period (i.e. t_j) under complex dynamic conditions. Let $\delta\mathbf{S}^j$ denote the observed vector error caused by complex motion, and Eq. (5) should be rewritten as:

$$\hat{\mathbf{S}}_j^N = \mathbf{G}_j^N \mathbf{S}^j + \mathbf{G}_j^N \delta\mathbf{S}^j + \mathbf{E}^j. \tag{6}$$

Accordingly, the attitude equation of the ACF approach (i.e. Eq. (3)) should be rewritten as:

$$\begin{cases} \left[\mathbf{P}^1, \mathbf{P}^2, \cdots, \mathbf{P}^N\right] = \mathbf{C}_N^i \left[\mathbf{G}_1^N \mathbf{S}^1, \mathbf{G}_2^N \mathbf{S}^2, \cdots, \mathbf{S}^N\right] + \\ \left[\mathbf{G}_1^N \delta\mathbf{S}^1, \mathbf{G}_2^N \delta\mathbf{S}^2, \cdots, \delta\mathbf{S}^N\right] + \left[\mathbf{E}^1, \mathbf{E}^2, \cdots, \mathbf{E}^N\right] \\ \mathbf{G}_j^N = \prod_{l=j}^{l=N-1} \mathbf{G}_l^{l+1}, j = 1, 2, \cdots, N-1 \end{cases}. \tag{7}$$

The CMIE are therefore introduced into the attitude equation, and will affect the attitude estimation accuracy of the ACF approach under complex dynamic conditions.

3. The centroid error compensation method under complex dynamic conditions

3.1. Compensation for the CMIE

Based on the analyses in Section 2, the CMIE affects the ACF performance under complex dynamic conditions. Therefore, the CMIE must be pre-compensated in order to improve the ACF accuracy in such conditions.

Since the centroid is indeed the integral of the star trajectory during the exposure period [13] and the star trajectory can be re-constructed through the GU outputs, the predicted star centroid contaminated by CMIE can be calculated. The measured star centroid represents the integral of true star motion acquired by the focal plane array detector. Thus, the difference between the predicted and measured star centroids reflects the CMIE [13].

Assuming that the time-dependent coordinate $[x(t), y(t)]$ indicates the true star trajectory in the p frame, and the measured star centroid can be expressed as [13]:

$$\begin{cases} X_m = \frac{1}{T}\int_{t_0}^{t_0+T} x(t)\,dt + \Delta X_m \\ Y_m = \frac{1}{T}\int_{t_0}^{t_0+T} y(t)\,dt + \Delta Y_m \end{cases}, \tag{8}$$

where, T is the exposure period, t_0 is the beginning of exposure period. ΔX_m and ΔY_m represent the centroid errors in X and Y directions respectively.

The predicted star centroid can be similarly expressed as:

$$\begin{cases} X_p = \frac{1}{T}\int_{t_0}^{t_0+T} \hat{x}(t)\,dt + \Delta X_p \\ Y_p = \frac{1}{T}\int_{t_0}^{t_0+T} \hat{y}(t)\,dt + \Delta Y_p \end{cases}, \tag{9}$$

where $[\hat{x}(t), \hat{y}(t)]$ indicates the predicted star trajectory.

Optics EXPRESS

Instantaneously, the true star vector $\mathbf{r}^s(t)$ and predicted star vector $\hat{\mathbf{r}}^s(t)$ in the s frame at time epoch t are given as:

$$\begin{cases} \mathbf{r}^s(t) = [-x(t), -y(t), f]^{\mathbf{T}} \\ \hat{\mathbf{r}}^s(t) = [-\hat{x}(t), -\hat{y}(t), f]^{\mathbf{T}}, \end{cases} \tag{10}$$

where f is the focal length of lens.

Similarly, the measured centroid vector $\mathbf{r}^s_{centroid}$ and the predicted centroid vector $\hat{\mathbf{r}}^s_{centroid}$ are given as:

$$\begin{cases} \mathbf{r}^s_{centroid} = [-X_m, -Y_m, f]^{\mathbf{T}} \\ \hat{\mathbf{r}}^s_{centroid} = [-X_p, -Y_p, f]^{\mathbf{T}}. \end{cases} \tag{11}$$

According to Eq. (11), the difference between the predicted centroid and the measured centroid is calculated as:

$$\Delta\mathbf{r} = \hat{\mathbf{r}}^s_{centroid} - \mathbf{r}^s_{centroid} = \begin{bmatrix} \Delta\mathbf{r}_x \\ \Delta\mathbf{r}_y \\ 0 \end{bmatrix} = \begin{bmatrix} X_m - X_p \\ Y_m - Y_p \\ 0 \end{bmatrix}. \tag{12}$$

Substituting Eq. (8) and Eq. (9) into the above equation, which is:

$$\Delta\mathbf{r} = \frac{1}{T}\int_{t_0}^{t_0+T} [\hat{\mathbf{r}}^s(t) - \mathbf{r}^s(t)]\, dt. \tag{13}$$

Considering star vectors at time epochs t and t_0, which satisfy:

$$\begin{cases} \hat{\mathbf{r}}^s(t) = \mathbf{C}^{s'(t)}_{s'(t_0)}\hat{\mathbf{r}}^s(t_0) \\ \mathbf{r}^s(t) = \mathbf{C}^{s(t)}_{s(t_0)}\mathbf{r}^s(t_0) \end{cases}, \tag{14}$$

where $\mathbf{C}^{s(t)}_{s(t_0)}$ and $\mathbf{C}^{s'(t)}_{s'(t_0)}$ represent the attitude transformations from time epoch t_0 to t in the star tracker coordinate system s and the computed star tracker coordinate system s' respectively. Thus, Eq. (13) can be expressed as:

$$\begin{aligned} \Delta\mathbf{r} &= \frac{1}{T}\int_{t_0}^{t_0+T} [\hat{\mathbf{r}}^s(t) - \mathbf{r}^s(t)]\, dt \\ &= \frac{1}{T}\int_{t_0}^{t_0+T} \left[\mathbf{C}^{s'(t)}_{s'(t_0)}\hat{\mathbf{r}}^s(t_0) - \mathbf{C}^{s(t)}_{s(t_0)}\mathbf{r}^s(t_0)\right] dt \\ &= \frac{1}{T}\int_{t_0}^{t_0+T} \left[\mathbf{C}^{s'(t)}_{s'(t_0)} - \mathbf{C}^{s(t)}_{s(t_0)}\mathbf{C}^{s(t_0)}_{s'(t_0)}\right] \hat{\mathbf{r}}^s(t_0) dt. \end{aligned} \tag{15}$$

When the angular velocity of the star tracker varies quickly, the attitude variation during the exposure period approaches infinity compared to the attitude error between frames s' and s (i.e. $\mathbf{C}^{s'(t)}_{s'(t_0)} \approx \mathbf{C}^{s(t)}_{s(t_0)}$). Eq. (15) can be approximately expressed as:

$$\Delta\mathbf{r} \approx \frac{1}{T}\int_{t_0}^{t_0+T} \mathbf{C}^{s(t)}_{s(t_0)} \left[\mathbf{I}_{3\times3} - \mathbf{C}^{s(t_0)}_{s'(t_0)}\right] \hat{\mathbf{r}}^s(t_0) dt, \tag{16}$$

where $\mathbf{I}_{3\times3}$ represents the identity matrix of size 3. Let $\boldsymbol{\phi} = [\phi_x, \phi_y, \phi_z]^{\mathbf{T}}$ denote the CMIE, which represents the Euler angle from s' frame to s frame at time epoch t_0. It can be accurately expressed in direction cosine matrix as:

$$\mathbf{C}^{s(t_0)}_{s'(t_0)} = \begin{bmatrix} cos\phi_y cos\phi_z - sin\phi_x sin\phi_y sin\phi_z & cos\phi_y sin\phi_z + sin\phi_x sin\phi_y cos\phi_z & -cos\phi_x sin\phi_y \\ -cos\phi_x sin\phi_z & cos\phi_x cos\phi_z & sin\phi_x \\ sin\phi_y cos\phi_z + sin\phi_x cos\phi_y sin\phi_z & sin\phi_y sin\phi_z - sin\phi_x cos\phi_y cos\phi_z & cos\phi_x cos\phi_y \end{bmatrix}. \tag{17}$$

In actual dynamic conditions of a star tracker, the CMIE is usually several hundreds of arc-seconds, which can be considered as a small-angle vector. According to small-angle approximation, the CMIE can be approximatively expressed as Eq. (18), and the approximation accuracy is less than 0.2" in typical dynamic conditions.

$$\mathbf{C}_{s'(t_0)}^{s(t_0)} \approx \mathbf{I}_{3\times3} - \begin{bmatrix} 0 & -\phi_z & \phi_y \\ \phi_z & 0 & -\phi_x \\ -\phi_y & \phi_x & 0 \end{bmatrix} = \mathbf{I}_{3\times3} - [\boldsymbol{\phi}\times]\,. \tag{18}$$

Substituting Eq. (18) into Eq. (16):

$$\begin{aligned} \Delta\mathbf{r} &= \frac{1}{T}\int_{t_0}^{t_0+T} \mathbf{C}_{s(t_0)}^{s(t)} dt [\boldsymbol{\phi}\times]\hat{\mathbf{r}}^s(t_0) \\ &= -\left(\frac{1}{T}\int_{t_0}^{t_0+T} \mathbf{C}_{s(t_0)}^{s(t)} dt\right)[\hat{\mathbf{r}}^s(t_0)\times]\boldsymbol{\phi} \\ &= -\left(\frac{1}{T}\int_{t_0}^{t_0+T} \mathbf{C}_g^s \mathbf{C}_{g(t_0)}^{g(t)} \mathbf{C}_s^g dt\right)[\hat{\mathbf{r}}^s(t_0)\times]\boldsymbol{\phi}, \end{aligned} \tag{19}$$

where $\mathbf{C}_g^s$ is the mount matrix from g frame to s frame, which can be calculated through previous calibration. $\mathbf{C}_{g(t_0)}^{g(t)}$ is the attitude transformation from time epoch t_0 to t in g frame, which can be calculated with the GU. $[\hat{\mathbf{r}}^s(t_0)\times]$ is the skew symmetric form of the predicted star vector at time epoch t_0 as:

$$[\hat{\mathbf{r}}^s(t_0)\times] = \begin{bmatrix} 0 & -f & -\hat{y}(t_0) \\ f & 0 & \hat{x}(t_0) \\ \hat{y}(t_0) & -\hat{x}(t_0) & 0 \end{bmatrix}. \tag{20}$$

Let

$$\mathbf{Z} = -\left(\frac{1}{T}\int_{t_0}^{t_0+T} \mathbf{C}_g^s \mathbf{C}_{g(t_0)}^{g(t)} \mathbf{C}_s^g dt\right)[\hat{\mathbf{r}}^s(t_0)\times], \tag{21}$$

and Eq. (19) can be simplified as:

$$\Delta\mathbf{r} = \mathbf{Z}\boldsymbol{\phi}. \tag{22}$$

Eq. (22) is deduced for each star across the star tracker's field of view (FOV). For a star frame with n_{star} stars, Eq. (22) can be extended as:

$$\mathbb{R} = \mathbb{Z}\boldsymbol{\phi}, \tag{23}$$

where $\mathbb{R} = \left[\Delta\mathbf{r}_1, \Delta\mathbf{r}_2, \cdots, \Delta\mathbf{r}_{n_{star}}\right]^{\mathbf{T}}$ and $\mathbb{Z} = \left[\mathbf{Z}_1, \mathbf{Z}_2, \cdots, \mathbf{Z}_{n_{star}}\right]^{\mathbf{T}}$. Here, $\Delta\mathbf{r}$ is the difference between the predicted star centroid and the measured star centroid expressed as Eq. (12). The predicted star centroid is calculated by the integral of the predicted star trajectory during the exposure period expressed by Eq. (9), and the measured star centroid is obtained by extracting the star centroid [16, 19] of the real star image. $\mathbf{Z}$ can be calculated through Eq. (20) and Eq. (21). Accordingly, $\boldsymbol{\phi}$ is the only unknown parameter in Eq. (23), and the least square solution of the above equation is:

$$\hat{\boldsymbol{\phi}} = (\mathbb{Z}^{\mathbf{T}}\mathbb{Z})^{-1}\mathbb{Z}^{\mathbf{T}}\mathbb{R}. \tag{24}$$

Hence, the CMIE can be estimated through Eq. (24), and it can be compensated by:

$$\tilde{\mathbf{C}}_s^i = (\mathbf{I} - [\boldsymbol{\phi}\times])\hat{\mathbf{C}}_s^i, \tag{25}$$

where $\hat{\mathbf{C}}_s^i$ is the attitude matrix contaminated by CMIE, and $\tilde{\mathbf{C}}_s^i$ is the attitude matrix free of CMIE. In particular, $\tilde{\mathbf{C}}_s^i$ points to the attitude matrix at the beginning of the exposure period as $\boldsymbol{\phi}$ denotes the Euler angle error at start time epoch t_0, and it will be used for the following procedures of attitude fusion and ACF approach further.

Optics EXPRESS

3.2. Observation sensitivity to CMIE and attitude fusion

In order to estimate $\boldsymbol{\phi}$ more effectively, the sensitivity of observation $\Delta\mathbf{r}$ to the sub-components of $\boldsymbol{\phi}$(i.e. ϕ_x,ϕ_y,ϕ_z) is analyzed.

Let

$$C = -\frac{1}{T}\int_{t_0}^{t_0+T} \mathbf{C}_g^s \mathbf{C}_{g(t_0)}^{g(t)} \mathbf{C}_s^g \, dt, \tag{26}$$

and Eq. (19) can be rewritten as:

$$\begin{aligned}\Delta\mathbf{r} &= C[\hat{\mathbf{r}}^s(t_0)\times]\boldsymbol{\phi} \\ &= \begin{bmatrix} C_{11} & C_{12} & C_{13} \\ C_{21} & C_{22} & C_{23} \\ C_{31} & C_{32} & C_{33} \end{bmatrix} \begin{bmatrix} 0 & -f & -\hat{y}(t_0) \\ f & 0 & \hat{x}(t_0) \\ \hat{y}(t_0) & -\hat{x}(t_0) & 0 \end{bmatrix} \boldsymbol{\phi} \\ &= \begin{bmatrix} C_{12}f + C_{13}\hat{y}(t_0) & -C_{11}f - C_{13}\hat{x}(t_0) & -C_{11}\hat{y}(t_0) + C_{12}\hat{x}(t_0) \\ C_{22}f + C_{23}\hat{y}(t_0) & -C_{21}f - C_{23}\hat{x}(t_0) & -C_{21}\hat{y}(t_0) + C_{22}\hat{x}(t_0) \\ C_{32}f + C_{33}\hat{y}(t_0) & -C_{31}f - C_{33}\hat{x}(t_0) & -C_{31}\hat{y}(t_0) + C_{32}\hat{x}(t_0) \end{bmatrix} \boldsymbol{\phi}, \end{aligned} \tag{27}$$

where $C_{ij}(i, j = 1, 2, 3)$ represent the elements of matrix C. In Eq. (27), $\Delta\mathbf{r}$ can be observed and $\boldsymbol{\phi}$ is unknown,which should be solved. The sensitivity of the observation is determined by the coefficient matrix in Eq. (27), which is related to the matrix elements $\mathbf{C}_{ij}$ calculated by Eq. (26). Since $\mathbf{C}_{ij}$ is calculated with GU angular velocity measurements during the exposure period, the coefficient matrix of Eq. (27) varies under different dynamic conditions.

To achieve the observation sensitivity to CMIE of a shipborne star tracker, simulations are performed under shipboard dynamic conditions. The angular velocity of the star tracker in simulation is shown in Fig. 2. This emulates conditions observed under true shipboard dynamic conditions. One thousand coefficient matrices are generated as a result with parameters listed in Table 1.

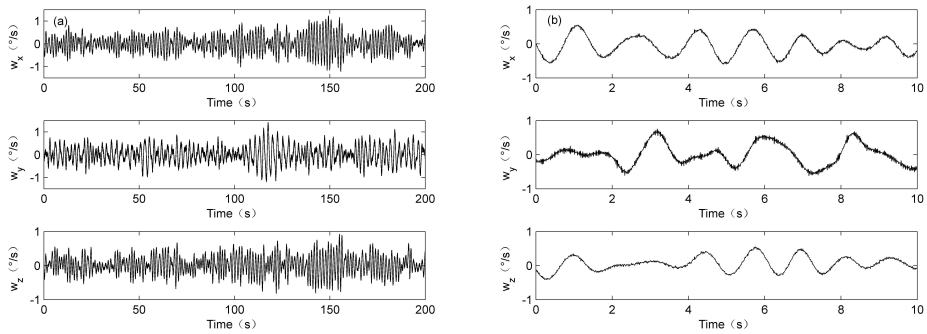

Fig. 2. Model of angular velocity w, in 3 axes over 200s (left) and 10s (right) used within simulations.

The simulation results are shown by the dotted curves in Fig. 3, which show the sensitivity of observation $\Delta\mathbf{r}$ to the CMIE $\boldsymbol{\phi}$. Each dot represents the root mean square of 1000 simulation results. Subfigures (a) and (b) show the sensitivities of $\Delta\mathbf{r}$ (including $\Delta\mathbf{r}_x$ and $\Delta\mathbf{r}_y$) to ϕ_x, subfigures (c) and (d) show the sensitivity of $\Delta\mathbf{r}$ to ϕ_y, and subfigures (e) and (f) show the sensitivity of $\Delta\mathbf{r}$ to ϕ_z. As shown in Fig. 3, the relationship between the variables in all subfigures is approximately linear. The gradients of the fitted curves are shown in Fig. 4. The gradients indicate the sensitivity of observation to the CMIE. In other words, the greater observation value, which is caused by the same error, means higher sensitivity. Accordingly, $\Delta\mathbf{r}_x$ and $\Delta\mathbf{r}_y$ are

Optics EXPRESS

Table 1. **Simulation parameters**

Parameter	Value	Parameter	Value
Active pixels	1024×1024	Exposure period	$180ms$
Pixel pitch	$6.45 \times 6.45\mu m^2$	Star tracker update frequency	$5Hz$
Noise gray level	40	Gyroscope sampling frequency	$100Hz$
Saturated gray level	65535	Gyroscope bias	$0.01°/h$
FOV	$14° \times 14°$	Gyroscope anglular random walk	$0.003°/\sqrt{h}$
Focal length	$25.6mm$		

sensitive to ϕ_y and ϕ_x respectively. However, neither $\Delta\mathbf{r}_x$ nor $\Delta\mathbf{r}_y$ is sensitive to ϕ_z. Specifically, the sensitivity of observation to ϕ_x and ϕ_y are more than 20 times higher than ϕ_z. In other words, the signal-noise ratio (SNR) of ϕ_z is much lower than ϕ_x or ϕ_y under the same noise level. This is because the focus dimension is about one order of magnitude larger than the detector dimension.

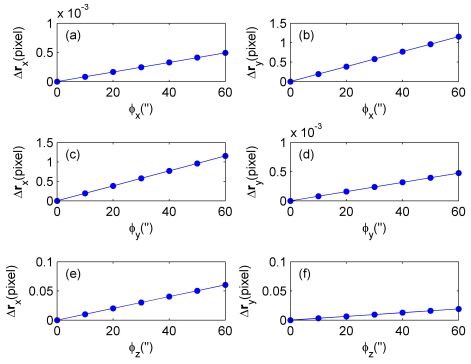

Fig. 3. The sensitivity of observation $\Delta\mathbf{r}$ to the CMIE $\boldsymbol{\phi}$. Subfigure axes have been scaled to highlight detail. (a) and (b) show the sensitivity of $\Delta\mathbf{r}$(including $\Delta\mathbf{r}_x$ and $\Delta\mathbf{r}_y$) to ϕ_x. (c) and (d) show the sensitivity of $\Delta\mathbf{r}$(including $\Delta\mathbf{r}_x$ and $\Delta\mathbf{r}_y$) to ϕ_y. (e) and (f) show the sensitivity of $\Delta\mathbf{r}$(including $\Delta\mathbf{r}_x$ and $\Delta\mathbf{r}_y$) to ϕ_z.

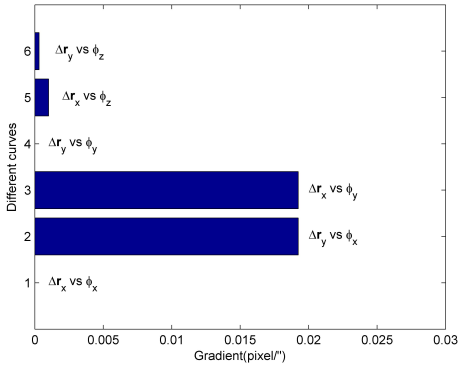

Fig. 4. Gradients of the fitted curves.

Accordingly, the subcomponents of the CMIE across boresight (i.e. ϕ_x, ϕ_y) can be estimated

Optics EXPRESS

and compensated with much higher accuracy than the subcomponent along the boresight direction (i.e. ϕ_z). Since the boresight error can be reduced effectively with a multi-FOV star tracker [20], attitudes from two different FOVs can be combined to increase the compensation accuracy of the CMIE along the boresight direction.

3.3. ACF approach for reducing the random error further

Since the CMIE can be well compensated through the above methods, the ACF performance will be improved under complex dynamic conditions as a result.

The flow chart of the proposed method is illustrated in Fig. 5. With a GU measuring the angular velocity of the star tracker, the CMIE is well compensated except ϕ_z. ϕ_z can be compensated through the combination of two different FOVs. Finally, the ACF approach is implemented.

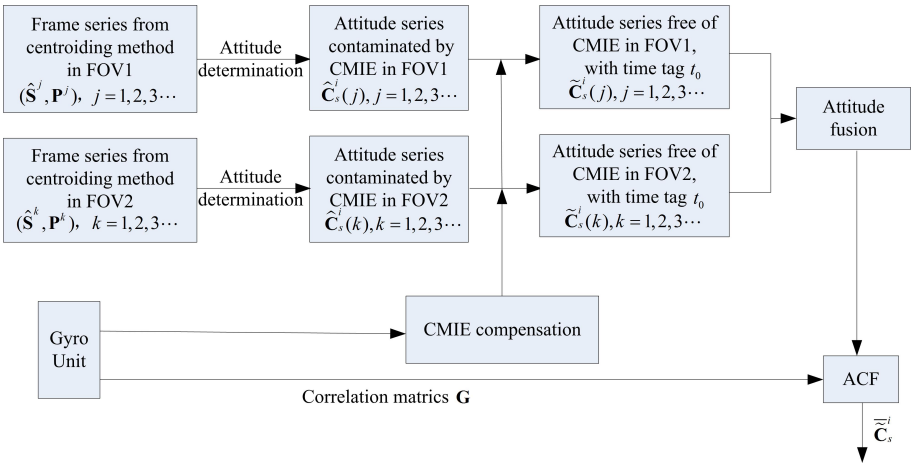

Fig. 5. Flowchart of the proposed method.

4. Simulation

In order to verify the effectiveness of the proposed method under complex dynamic conditions, simulations of attitude variation due to shipboard dynamic conditions were made. The angular velocity of the star tracker in simulation is shown in Fig. 2. This emulates conditions observed under true shipbord dynamic conditions. One thousand dynamic star images were generated with the same simulation parameters listed in Table 1. Fig. 6 shows an example of the generated star under shipboard dynamic conditions using the dynamic imaging model in [21].

The performance of three methods are compared from two aspects: the effectiveness of the compensation to CMIE and the improvement on the ACF approach. The three methods are listed as follows:

Method one (M1): The centroiding method shown as black curves in subsequent figures.

Method two (M2): The centroiding method with the CMIE compensated for single FOV shown as red curves.

Method three (M3): The centroiding method with the CMIE compensated, and attitudes from two different FOVs are combined shown as green curves.

As shown in Fig. 2, the angular velocity changes with time during the exposure period. The CMIE exists in the raw attitude results from the centroiding method, and the attitude error along different axes (i.e. x, y and z) are given by the black curves in Fig. 7. Attitude errors of M2 and M3 are given by red and green curves respectively. The statistical accuracy (RMS error) of the three methods are shown in Table 2. Here, the number of frame N is 1 (i.e. The ACF approach is

Optics EXPRESS

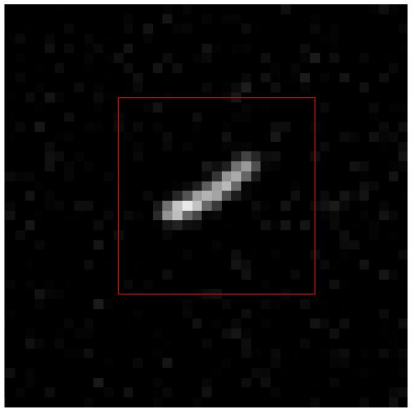

Fig. 6. Simulated star under shipboard dynamic conditions.

not applied yet). Compared to M1, the performance of M2 improves by 82.3% across boresight direction but only 6.0% along boresight direction. The performance improvements of M3 are 83.1% across boresight direction and 84.5% along boresight direction respectively. Obviously, M2 is effective in compensating the cross boresight component of the CMIE but deficient for the component along the boresight direction, which coincides with the theoretical analyses above. M3 can overcome the shortage of M2, which means that the CMIE can be compensated completely both across and along the boresight directions.

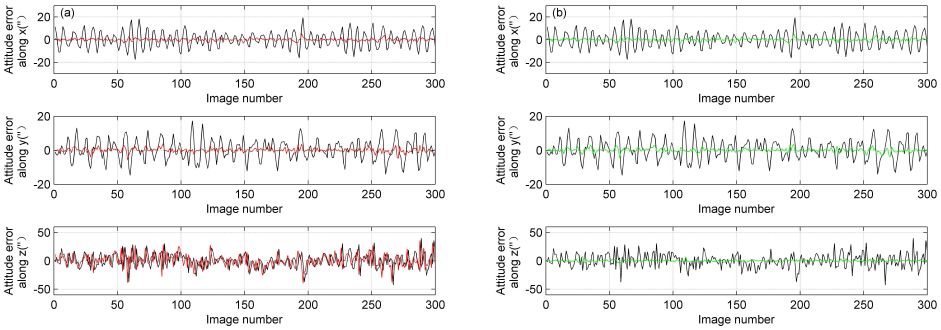

Fig. 7. Simulation results of compensation of CMIE, and only 300 of all the emulated frames are plotted in order to display fine details. (a) The black curve is the attitude error of the centroiding method, and the red curve is the attitude error where the CMIE has been compensated for single FOV. (b) The black curve is the attitude error of the centroiding method, and the green curve is the attitude error where the CMIE has been compensated and the attitudes from different FOVs have been combined.

Then the ACF algorithm is applied to M1, M2 and M3 respectively, and the number of frames N is sequentially set to $2, \cdots, 10$. An example of the attitude error curve with $N = 9$ is shown in Fig. 8. Obviously, the attitude error curve becomes much smoother with the ACF approach. The statistical accuracy of the ACF approach is shown in Fig. 9. M3 shows a better performance, which means the ACF performance is improved under complex dynamic conditions. The comparison between the proposed method and the theoretical curve $1/\sqrt{N}$ is shown in Fig. 9(b), and the

Optics EXPRESS

Table 2. **Statistical results of different compensation methods in the simulation (N=1, which means ACF is not applied)**

	M1	M2	M3
ϕ_x(")	8.75	1.37	1.37
ϕ_y(")	6.52	1.36	1.24
ϕ_z(")	13.91	13.07	2.16

maximum deviation from the theoretical curve is approximately 0.1".

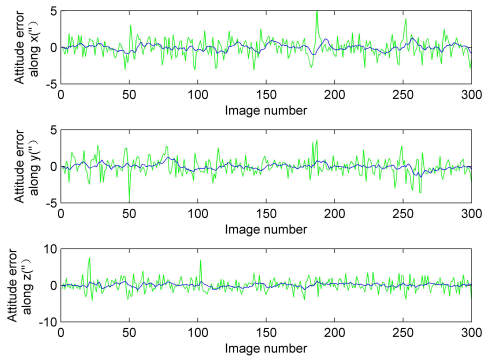

Fig. 8. Simulation results of attitude error of the proposed method when N = 9. The green curve is the same as that in Fig. 7(b), and the blue curve is the result of the ACF approach when the number of frames N is 9.

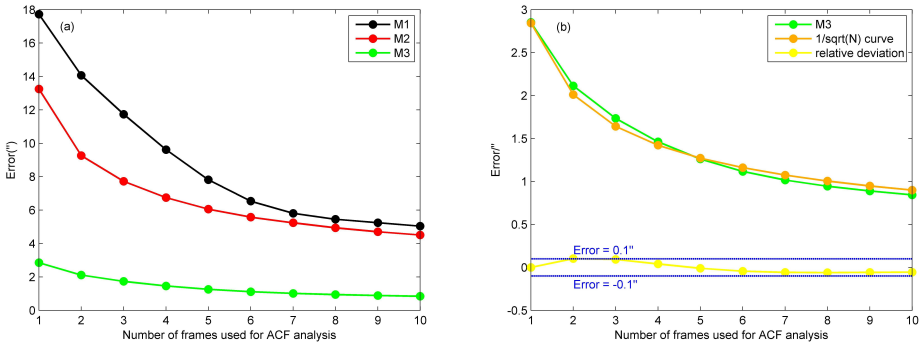

Fig. 9. Statistical results of the ACF approach. (a) The curves with different colors are the attitude errors with different methods. The dotted curves with the same color are the attitude errors under different number of frames N. The black curve represents the accuracy of the ACF approach on the raw data of centroiding method. The red curve represents the accuracy of the ACF approach, where the CMIE has been compensated for a single FOV. The green curve represents the accuracy of the ACF approach, where the CMIE has been compensated and the attitudes from different FOVs have been combined. (b) The green curve is the statistical results of the proposed method, which is the same as the curve with the same color in Part (a). The brown curve is the theoretical curve $1/\sqrt{N}$. The yellow curve shows the relative deviation of the above two curves.

Optics EXPRESS

5. Experiment

Some experiments were conducted to verify the proposed method at the summit of Daweishan National Forest Park (Changsha, China). The equipments used in experiments are shown in Fig. 10. The star tracker and INS (with GU inside) are fixed together so that the angular velocity sensed by the GU can be transformed to the s frame through the pre-calibrated mount matrix $\mathbf{C}_g^s$. The performance specifications of the star tracker used are consistent with previous simulation parameters.

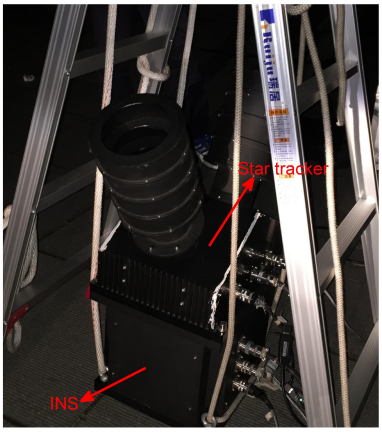

Fig. 10. Experimental setup.

Since the proposed method is particularly suitable for complex dynamic conditions, a simple experimental setup (shown in Fig. 10) is adopted to keep the angular velocity of the system varying continuously. By hanging the star tracker and GU integrated system off the ground, the system will oscillate after initial excitation. The angular velocity of the star tracker in the experiment is shown in Fig. 11. According to the enlarged detail, the angular velocity of the system varies continuously during the exposure period.

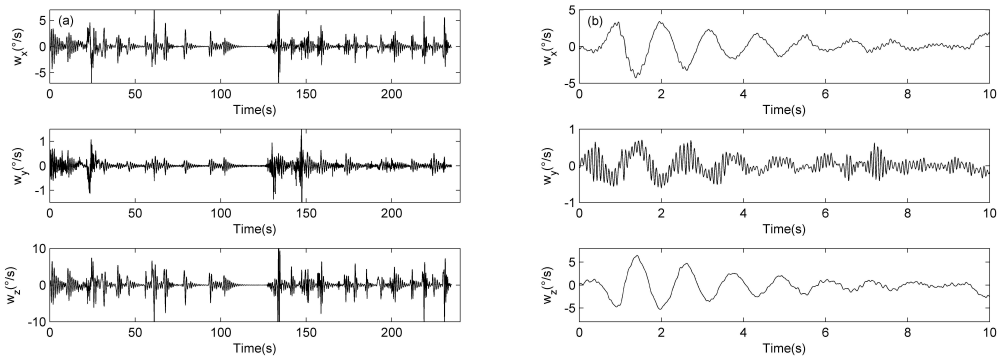

Fig. 11. Three-axes angular velocity of the star tracker. Part (b) is partial enlarged detail of (a) in order to display fine details.

Since the accuracy of the gyroscope is approximately $0.01°/h$ in the experiment, it can be

Optics EXPRESS

applied to evaluate the relative attitude accuracy of the star tracker. The relative attitude accuracies of M1, M2 and M3 are shown by curves with different colors in Fig. 12, respectively. The statistical accuracy (RMS error) of the three methods are shown in Table 3. Here, the number of frames N is 1 (i.e. The ACF approach is not applied yet). Compared to M1, the performance of M2 improves by 54.4% across the boresight direction but only 12.3% along the boresight direction. The performance improvements of M3 are 53.9% across the boresight direction and 85.1% along the boresight direction respectively. Obviously, M2 is effective in compensating the cross boresight component of the CMIE but deficient for the component along the boresight direction, which coincides with the theoretical analyses and simulations above. M3 can overcome the shortfall of M2, which means that the CMIE can be compensated completely both across and along the boresight directions.

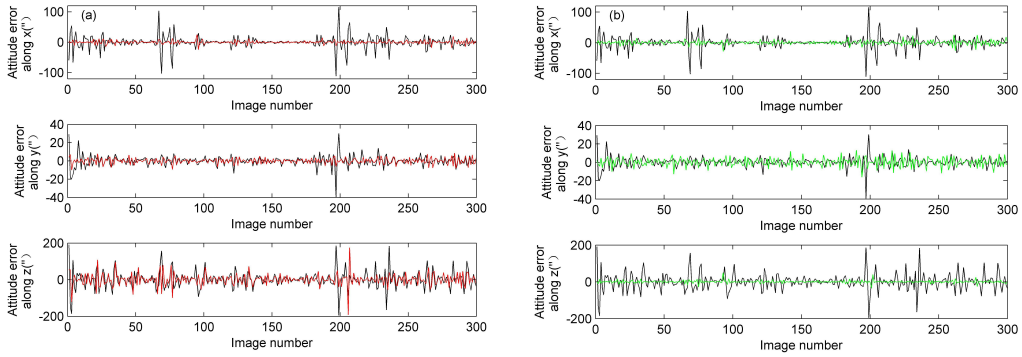

Fig. 12. Experimental results of compensation of CMIE. (a) The black curve is the attitude error of the centroiding method, and the red curve is the attitude error where the CMIE has been compensated for single FOV. (b) The black curve is the attitude error of the centroiding method, and the green curve is the attitude error where the CMIE has been compensated and the attitudes from different FOVs have been combined.

Table 3. **Statistical results of different compensation methods in the experiment (N=1, which means ACF is not applied)**

	M1	M2	M3
ϕ_x(")	16.71	6.92	6.52
ϕ_y(")	5.80	4.13	4.91
ϕ_z(")	41.73	36.59	6.21

Then the ACF algorithm is applied to M1, M2 and M3 respectively, and the number of frames N is sequentially set to $2, 3, 4, \cdots, 10$. An example of the relative attitude error curve with $N = 9$ is shown in Fig. 13. Obviously, the relative attitude error curve becomes much smoother with the ACF approach. The statistical accuracy of the ACF approach is shown in Fig. 14(a). M3 shows a better performance, which means the ACF performance is improved under complex dynamic conditions. The comparison between the proposed method and the theoretical curve $1/N$ is shown in Fig. 14(b) (The theoretical curve of the ACF approach for relative attitude accuracy of adjacent frames is $1/N$, which is different from the curve $1/\sqrt{N}$ for the absolute attitude accuracy in the simulation), and the maximum deviation from the theoretical curve is approximately 0.9".

Optics EXPRESS

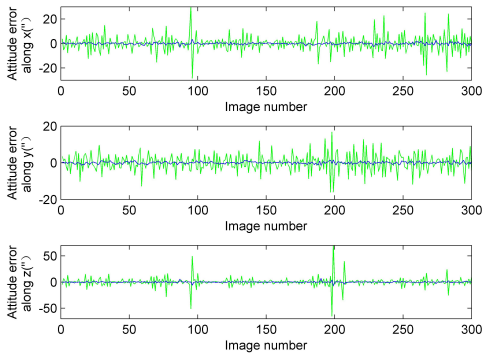

Fig. 13. Experimental results of the relative attitude error of the proposed method when $N = 9$. The green curve is the same as that in Fig. 12(b), and the blue curve is the result of the ACF approach when the number of frames N is 9.

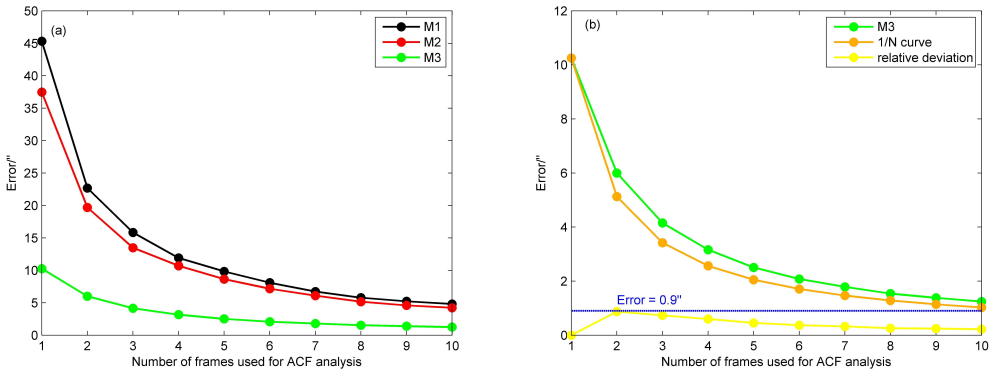

Fig. 14. Statistical results of the ACF approach. (a) The curves with different colors are the attitude errors with different methods. The dotted curves with the same color are the attitude errors under different number of frames N. The black curve represents the accuracy of the ACF approach on the centroiding data. The red curve represents the accuracy of the ACF approach, where the CMIE has been compensated for a single FOV. The green curve represents the accuracy of the ACF approach, where the CMIE has been compensated and the attitudes from different FOVs have been combined. (b) The green curve is the statistical results of the proposed method, which is the same as the curve with the same color in Part (a). The brown curve is the theoretical curve $1/N$. The yellow curve shows the relative deviation of the above two curves.

6. Conclusions

Considering the deficiency of the ACF approach under complex dynamic conditions, a method for compensating the CMIE of the star tracker in such conditions is proposed, which is also applied to the ACF approach to improve its performance. Simulations under shipboard dynamic conditions were made. The absolute attitude errors across and along boresight directions improve by 83.1% and 84.5% respectively through performing CMIE compensation. The maximum deviation of the ACF statistical accuracy curve from the theoretical curve is approximately 0.1". Experiments under oscillation dynamic conditions show that the relative attitude errors across and along boresight directions improve by 53.9% and 85.1% respectively through performing CMIE

Optics EXPRESS

compensation. The maximum deviation of the ACF statistical accuracy curve from the theoretical curve is approximately 0.9". Therefore, the proposed method is effective in compensating the CMIE under complex dynamic conditions, and the performance of the ACF approach in such conditions is improved as well. The application fields of the ACF approach are expanded as a result.

The method can be applied to the star tracker and INS integrated navigation system directly. INS can provide accurate inertial information for this method. In turn, the accumulating error of the inertial navigation system can be better estimated with more accurate attitudes of vehicles under complex dynamic conditions.

Funding

National Natural Science Foundation of China (NSFC) (61573368,11172323,61275002).